ELSEVIER

Volume 182, Number 7, July 2009

JOURNAL OF SOLID STATE CHEMISTRY

www.elsevier.com/locate/jssc

CONTENTS

Abstracted/indexed in BioEngineering Abstracts, Chemical Abstracts, Coal Abstracts, Current Contents/Physics, Chemical, & Earth Sciences, Engineering Index, Research Alert, SCISEARCH, Science Abstracts, and Science Citation Index. Also covered in the abstract and citation database SCOPUS®. Full text available on ScienceDirect®.

Regular Articles

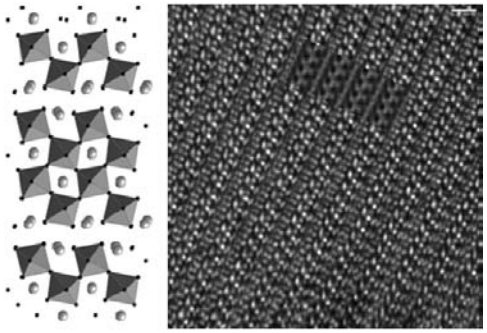

Epitaxial thin films of $RE_2Ti_2O_7$ (RE = Gd, Sm, Nd, and La) were deposited on single crystal $SrTiO_3$ (110) substrates using pulsed laser deposition (PLD). All compositions adopted the monoclinic (110)-layered perovskite structure, which is the stable phase for $La_2Ti_2O_7$ and $Nd_2Ti_2O_7$ but is metastable with respect to the pyrochlore phase for $Sm_2Ti_2O_7$ and $Gd_2Ti_2O_7$.

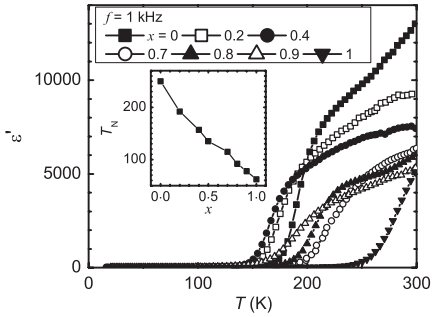

Dielectric constant (ε') and magnetic transition temperature (T_N) of $YbFe_{2-x}Mn_xO_4$ ($0 \leqslant x \leqslant 1$), which is a solid-solution system of new multiferroic oxides RFe_2O_4 (R = Y, Ho–Lu).

Regular Articles—Continued

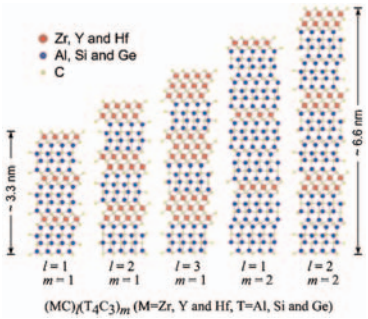

The layered carbide $(Zr_{0.72}Y_{0.28}C)Al_4C_3$ has been synthesized and found to be a new member with l = 1 and m = 1 of the homologous series $(MC)_l(T_4C_3)_m$ (l = 1, 2 and 3, m = 1 and 2, M = Zr, Y and Hf, T = Al, Si and Ge).

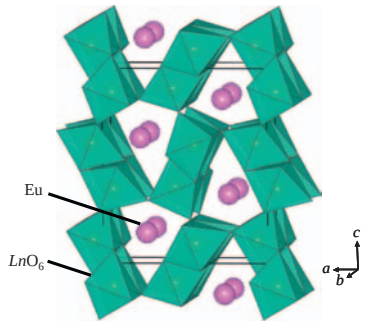

Ternary rare earth oxides $EuLn_2O_4$ (Ln = Gd, Dy-Lu) crystallized in an orthorhombic $CaFe_2O_4$-type structure with space group Pnma. Mössbauer spectroscopic measurements show that the Eu ions are in the divalent state. All these compounds show an antiferromagnetic transition at 4.2–6.3 K. It is considered that ferromagnetic chains of Eu^{2+} are aligned along the b-axis of the orthorhombic unit cell, with neighboring Eu^{2+} chains antiparallel.

Continued

Mesoporous hybrids containing Eu^{3+} complexes covalently bonded to SBA-15 functionalized: Assembly, characterization and photoluminescence

Li Li Kong, Bing Yan and Ying Li

Page 1631

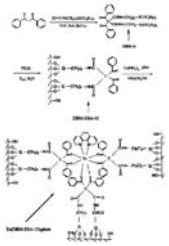

A novel organic–inorganic mesoporous luminescent hybrid materials is prepared by linking the binary and ternary Eu^{3+} complexes to the functionalized ordered mesoporous SBA-15 with the modified 1,3-diphenyl-1,3-propanepione (DBM) via a co-condensation process of tetraethoxysilane (TEOS) in the presence of Pluronic P123 surfactant as a template.

Structural and magnetic properties of $Pr_{18}Li_8Fe_{5-x}M_xO_{39}$ (M = Ru, Mn, Co)

Siân E. Dutton, Peter D. Battle, Fernande Grandjean, Gary J. Long, Moulay T. Sougrati, Peter A. van Daesdonk and Emma Winstone

Page 1638

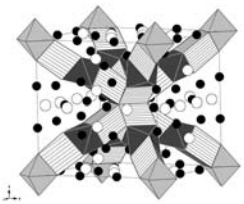

$Pr_{18}Li_8Fe_{5-x}M_xO_{39}$ (M = Ru, Mn, Co) have been studied by neutron diffraction, Mössbauer spectroscopy and magnetometry, allowing the distribution of the different cation species over the octahedral and trigonal-prismatic coordination sites within the structure to be determined. All the compositions studied undergo a transition to a spin-glass-like phase on cooling below ~5 K.

Functionalized mesoporous materials for adsorption and release of different drug molecules: A comparative study

Gang Wang, Amy N. Otuonye, Elizabeth A. Blair, Kelley Denton, Zhimin Tao and Tewodros Asefa

Page 1649

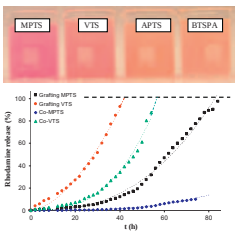

The adsorption capacity and release properties of mesoporous materials for various drug molecules are tuned by functionalizing the surfaces of the materials with judiciously chosen organic groups. This work reports comparative studies of the adsorption and release properties of functionalized ordered mesoporous materials containing different hydrophobic and hydrophilic groups that are synthesized via a co-condensation and post-grafting methods for various model drug molecules.

Fabrication of $Cs_{2.5}H_{0.5}PW_{12}O_{40}$ three-dimensional ordered film by colloidal crystal template

Fang Chai, Dongliu Li, Hongbo Wu, Chunli Zhang and Xiaohong Wang

Page 1661

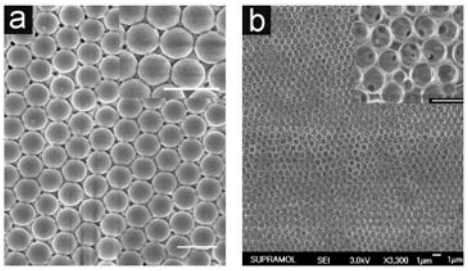

A three-dimensional ordered $Cs_{2.5}H_{0.5}PW_{12}O_{40}$ periodic film was synthesized by an inverse opal method using $H_3PW_{12}O_{40}$ and Cs_2CO_3 as precursors via nanocasting route and colloidal crystal as template (all scale bars are 1 μm).

Structural investigation of $K_xBa_{1-x}Ga_{2-x}Ge_{2+x}O_8$ solid solutions using the X-ray Rietveld method

Ni Qin, Marjeta Maček Kržmanc, Anton Meden and Danilo Suvorov

Page 1666

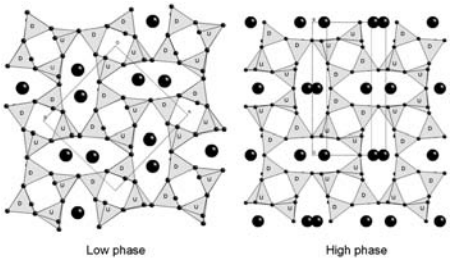

The $K_xBa_{1-x}Ga_{2-x}Ge_{2+x}O_8$ (x = 0.6–1.0) solid solutions undergo a structural phase transition. The crystal structures of both phases within the solid-solution region were determined by the Rietveld method using powder X-ray diffraction data. The topological analogy between the two structures is seen by comparing the (001) projections of the low phase structure (left) and the (20$\bar{1}$) projection of the high phase structure (right).

Reduction of Eu^{3+} to Eu^{2+} in $MAl_2Si_2O_8$ (M = Ca, Sr, Ba) in air condition

Cuimiao Zhang, Jun Yang, Cuikun Lin, Chunxia Li and Jun Lin

Page 1673

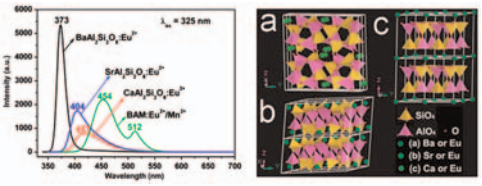

It is of great importance to find that the reduction of Eu^{3+} to Eu^{2+} can be realized in a series of alkaline-earth metal aluminum silicates $MAl_2Si_2O_8$ (M = Ca, Sr, Ba) just in air condition.

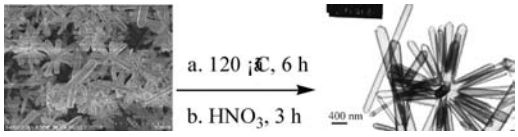

Tubular silica was prepared via a hydrothermal reaction between $BaSiF_6$ and NaOH, in which $BaSiF_6$ nanorods act as both a physical and chemical template. It was found that the amount of NaOH, reaction temperature, and reaction time played important roles in this transformation process.

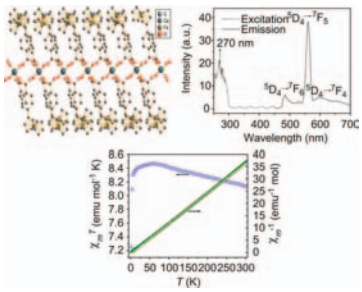

Seven *p*-ferrocenylbenzoate lanthanide coordination polymers were synthesized. Given is the perspective view of a unique 1D double-bridged infinite chain structure of 1, excitation and emission spectra of 6 and plots of $\chi_m T$ vs. T and χ_m^{-1} vs. T of 5.

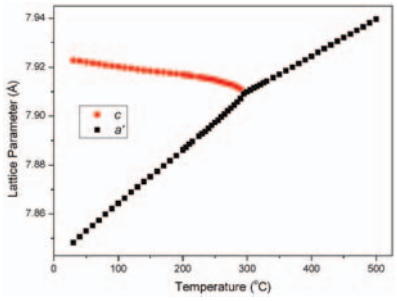

The crystal structure of polycrystalline Sr_2LiReO_6 from room temperature 30 to 500 °C is described. The sample undergoes a continuous and second order $I4/m$ to $Fm\bar{3}m$ phase transition. This transition is reversible and the tetragonal structure is formed upon re-cooling the cubic form.

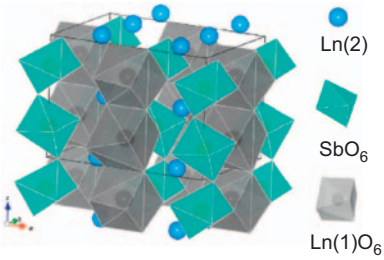

Ternary rare earth antimonates Ln_3SbO_7 (Ln = rare earths) crystallize in an orthorhombic superstructure of cubic fluorite (space group $Cmcm$ for Ln = La, Pr, Nd; $C222_1$ for Ln = Nd–Lu), in which Ln^{3+} ions occupy two different crystallographic sites (the 8-coordinated and 7-coordinated sites). Any of these compounds Ln_3SbO_7 (Ln = Nd, Gd–Ho) shows an antiferromagnetic transition at 2.2–3.2 K.

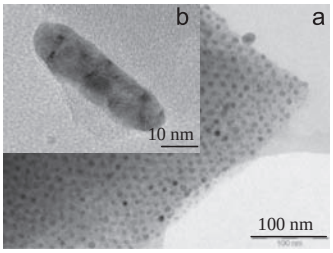

Growth of silver nanoparticles in a mesostructured block copolymer F127-silica film is performed either by a chemical route involving $NaBH_4$ reduction or by a thermal method. An array of spherical silver nanoparticles with 10 nm diameter on the upper-side of the mesostructured film or silver sticks long of 40 nm with a preferential orientation are obtained according to the method used. a: TEM image of the Fag5SiNB sample illustrating the silver nanoparticles array obtained by the chemical process; b: HR-TEM image of the Fag20Sid2 sample illustrating the silver nanosticks obtained by the thermal process.

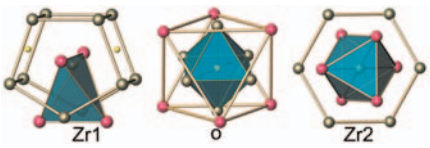

The figure shows the environments of three atom types in the corrected structure, an oxygen-stuffed Ti_2Ni type.

Continued

Oxygen-vacancy concentration in $A_2MgMoO_{6-\delta}$ double-perovskite oxides

Y. Matsuda, M. Karppinen, Y. Yamazaki and H. Yamauchi

Page 1713

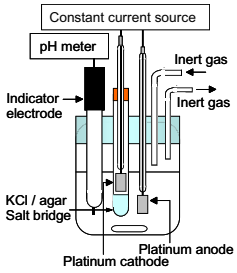

A highly reproducible coulometric redox titration method has been developed to accurately analyze the mixed V/VI valence state of molybdenum and thereby the oxygen content in the recently reported SOFC-anode materials of $A_2MgMoO_{6-\delta}$.

Crystal structures and phase transitions of Sr_2CrSbO_6

A. Faik, J.M. Igartua, M. Gateshki and G.J. Cuello

Page 1717

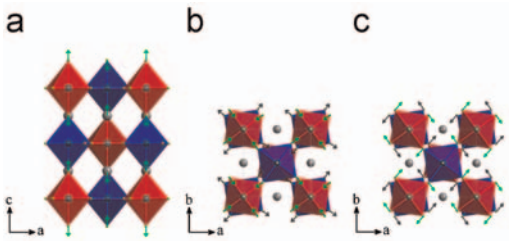

The components of the GM^{3+} mode, responsible for the breaking of the symmetry to the $I4/mmm$ tetragonal space group from the $Fm\text{-}3m$, observed experimentally at high. This mode involves the movements of all the oxygen atoms in the octahedra: those located in the $(00z)$ positions move to the center (or out of) of the octahedra, as shown in (a); and the oxygen atoms located in the xy plane move outwards (inwards) along the diagonals of the basal plane of the octahedra (b). As the octahedra are corner sharing if one octahedra stretches the other one expands. (c) On the other hand, the mode GM^{4+} is responsible for the breaking of the symmetry down to the $I4/m$ space group, and involves movements only of the oxygen atoms located in the xy plane (c): those displacements can be viewed as rotations (tilts) of the octahedra around the tetragonal axis.

Synthesis and characterization of Cr-MSU-1 and its catalytic application for oxidation of styrene

Hong Liu, Zhigang Wang, Hongjiu Hu, Yuguang Liang and Mengyang Wang

Page 1726

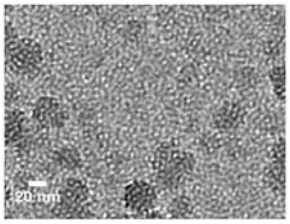

Mesoporous Cr-MSU-1 with worm-like holes was synthesized by a novel two-step method. The Cr-MSU-1 material is highly active and stable for the selective oxidation of styrene.

Porosity control in nanoporous carbide-derived carbon by oxidation in air and carbon dioxide

S. Osswald, C. Portet, Y. Gogotsi, G. Laudisio, J.P. Singer, J.E. Fischer, V.V. Sokolov, J.A. Kukushkina and A.E. Kravchik

Page 1733

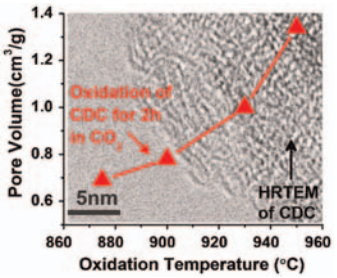

Carbide-derived carbons (CDC) provide great potential for sorption of toxicants and gas storage applications. Activation of CDC in air and CO_2 at different temperatures and times is applied in order to maximize pore volume and specific surface area, and control the average pore size with subnanometer accuracy.

Influence of electrospraying parameters on the microstructure of $La_{0.6}Sr_{0.4}Co_{0.2}F_{0.8}O_{3-\delta}$ films for SOFCs

Daniel Marinha, Cécile Rossignol and Elisabeth Djurado

Page 1742

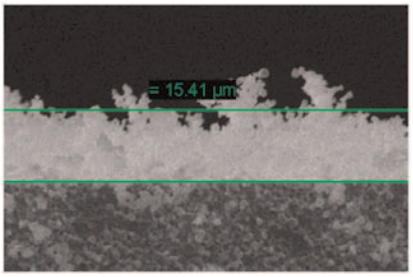

This work is devoted to the fabrication of $La_{0.6}Sr_{0.4}Co_{0.2}Fe_{0.8}O_{3-\delta}$ films on dense $Ce_{0.9}Gd_{0.1}O_{2-\delta}$ substrates by electrostatic spray deposition (ESD) and to the characterization of the microstructural dependence on the deposition conditions. A wide variety of microstructures ranging from dense to porous, with particular features such as reticulation and micro-porosity, were obtained by varying the nozzle-to-substrate distance, substrate temperature and solution flow rate. Cross-section view of the fractal-like $La_{0.6}Sr_{0.4}Co_{0.2}Fe_{0.8}O_{3-\delta}$ cathode film, as-deposited by electrostatic spray deposition.

Synthesis of Na-A and/or Na-X zeolite/porous carbon composites from carbonized rice husk

Hiroaki Katsuki and Sridhar Komarneni

Page 1749

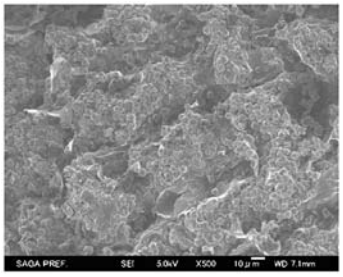

Novel Na-X zeolite/porous carbon composite.

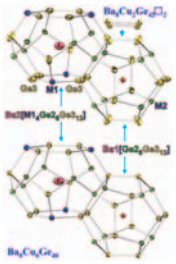

Cages and atom thermal displacement parameters in clathrate $Ba_8Cu_xGe_{46-x-y}\square_y$ for $Ba_8Cu_2Ge_{42}\square_2$ and $Ba_8Cu_6Ge_{40}$.

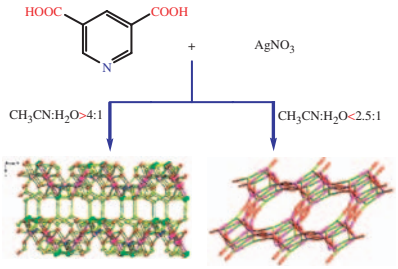

Hydrothermal reactions of pyridine-3,5-dicarboxylic acid (H_2pydc) with $AgNO_3$ at different preparing conditions lead to the formations of two three-dimensional network complexes. The luminescent properties have also been investigated.

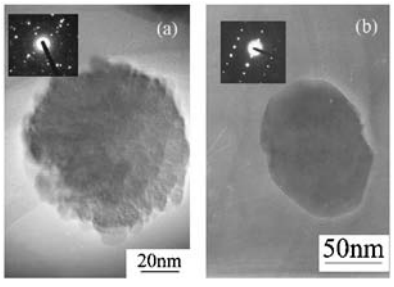

Ferrihydrites prepared by mixing Fe^{3+} and NaOH solutions according to different procedures can rapidly transform into hematite particles with different surface structures in the presence of trace Fe(II).

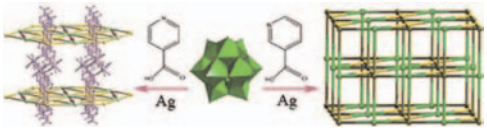

Two high-dimensional and highly connected α-metatungstate-compounds modified by Ag^I–HINA/HNA TMCs were successful obtained and the effect of isomeric organic ligands on the structures was systematically elucidated.

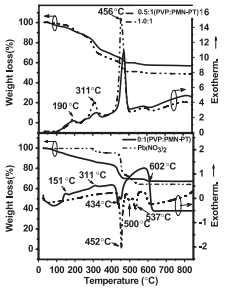

A polyvinylpyrrolidone modified sol–gel processing was developed to synthesize pure-perovskite $Pb(Mg_{1/3},Nb_{2/3})O_3$–$PbTiO_3$ films via bypassing pyrochlore phase.

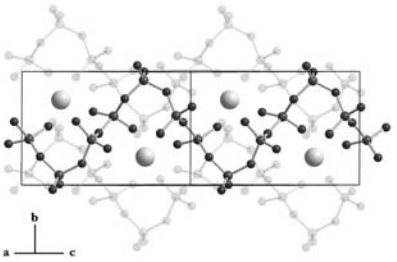

Basic structure from which all crystal structures of the late lanthanoids' polyphosphates at room temperature and below can be derived.

Continued

Disordered pyrochlore $CsMgInF_6$ at high pressures
Andrzej Grzechnik, Wolfgang Morgenroth and Karen Friese
Page 1792

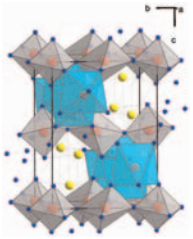

Crystal structure of $CsMgInF_6$ (*Pnma*, $Z=4$) at 6.04 GPa. Yellow, red, and blue symbols represent the Cs, (Mg/In), and F atoms, respectively. Octahedra around the (In1/Mg1) and (In2/Mg2) atoms are drawn gray and cyan, respectively.

Hydrothermal syntheses, crystal structures and properties of 0-D, 1-D and 2-D organic–inorganic hybrid borotungstates constructed from Keggin-type heteropolyanion $[\alpha\text{-}BW_{12}O_{40}]^{5-}$ and transition-metal complexes
Junwei Zhao, Yiping Song, Pengtao Ma, Jingping Wang and Jingyang Niu
Page 1798

Three novel organic–inorganic hybrid borotungstates $\{[Ni(phen)_2(H_2O)]_2H(\alpha\text{-}BW_{12}O_{40})\}\cdot 4H_2O$ (**1**), $[Cu^{I}(2,2'\text{-bipy})\ (4,4'\text{-bipy})_{0.5}]_2\{[Cu^{I}(2,2'\text{-bipy})]_2Cu^{I}(4,4'\text{-bipy})_2(\alpha\text{-}BW_{12}O_{40})\}$ (**2**) and $\{[Cu^{I}(4,4'\text{-bipy})]_3H_2(\alpha\text{-}BW_{12}O_{40})\}\cdot 3.5H_2O$ (**3**) have been hydrothermally synthesized and structurally characterized by single-crystal X-ray diffraction, thermogravimetric analyses, X-ray photoelectron spectroscopy and photoluminescence.

Polymorphism of the iron doped strontium aluminate $SrAl_{1.5}Fe_{0.5}O_4$
H. Desmoulins, S. Malo, S. Boudin, V. Caignaert and M. Hervieu
Page 1806

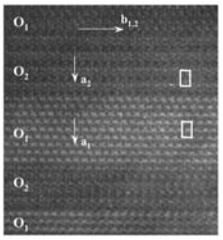

Four tridymite derivative structures $SrAl_{1.5}Fe_{0.5}O_4$ have been characterized. Two phases are isotypes of those observed for $SrAl_2O_4$. Two "orthorhombic" original phases are characterized by superstructures. The transitions between the different phases follow topotactic mechanisms. The transition LT→HT takes place from 620 to 1120 °C, explained by complex microstructures, creating ill-defined energy barriers.

Building thiol and metal-thiolate functions into coordination nets: Clues from a simple molecule
Jun He, Chen Yang, Zhengtao Xu, Matthias Zeller, Allen D. Hunter and Jianhua Lin
Page 1821

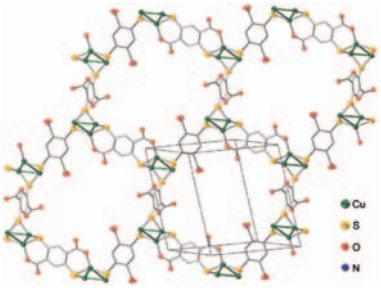

Molecule 2,5-dimercapto-1,4-benzenedicarboxylic acid was reacted with Cu^{+}, Pb^{2+} and Eu^{3+} ions to explore solid state networks with the rich structural features arising from the carboxyl-thiol combination.

Structure, magnetic and electrical properties of CeIrSb and its hydride $CeIrSbH_{0.8}$
Etienne Gaudin, Bernard Chevalier, Wilfried Hermes, Ute Ch. Rodewald and Rainer Pöttgen
Page 1827

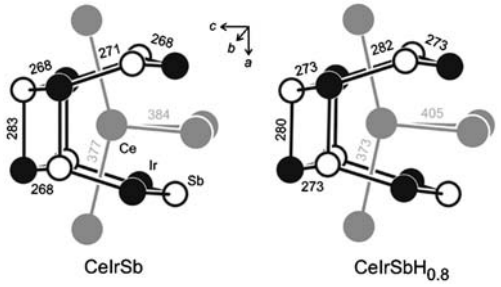

Cerium coordination in CeIrSb and $CeIrSbH_{0.8}$.

YMgGa as a hydrogen storage compound
Martin Sahlberg, Claudia Zlotea, Pietro Moretto and Yvonne Andersson
Page 1833

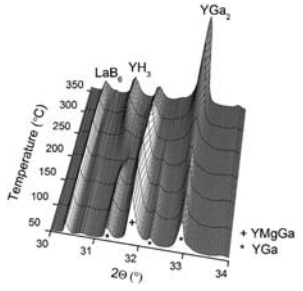

Hydrogen absorption in YMgGa studied by *in situ* powder X-ray diffraction. The hydrogen absorption and desorption properties were investigated by thermal desorption spectra and pressure-composition isotherms.

Doped titanium dioxide nanocrystalline powders with high photocatalytic activity
A.L. Castro, M.R. Nunes, M.D. Carvalho, L.P. Ferreira, J.-C. Jumas, F.M. Costa and M.H. Florêncio
Page 1838

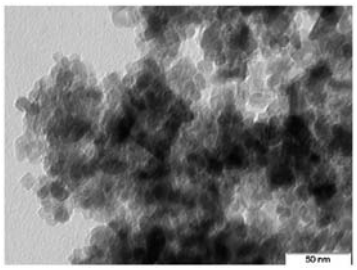

Doped titanium dioxide nanopowders (M:TiO_2; M = Fe, Co, Nb, Sb) with highly stable anatase structure were successfully synthesized through an hydrothermal route. The photocatalytic efficiencies of the synthesized nanopowders were tested and the results show an appreciable enhancement in the photoactivity of the Sb:TiO_2 and Nb:TiO_2.

Incommensurately modulated LT″-$Ni_{1+\delta}Sn$ ($\delta = 0.60, 0.63$): Rietveld refinement, line-broadening analysis and structural relation with LT- and LT′-$Ni_{1+\delta}Sn$
A. Leineweber
Page 1846

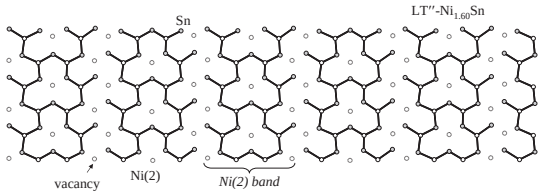

Approximant structure of incommensurately modulated LT″–$Ni_{1.60}Sn$, forming below 573 K from the disordered phase. The phase has a close structural relationship to the LT and LT′ phases occurring at lower Ni contents.

First-principles study of the electronic structures of α-rhombohedral boron codoped with lithium and oxygen
Wataru Hayami and Shigeki Otani
Page 1856

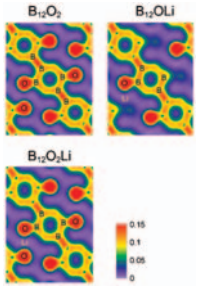

Density of electrons of $B_{12}O_2$, $B_{12}OLi$ and $B_{12}O_2Li$. The unit is electron/(a.u.)^3.

Synthesis and characterization of the new uranium yttrium oxysulfide $UY_4O_3S_5$
Geng Bang Jin, Eun Sang Choi, Daniel M. Wells and James A. Ibers
Page 1861

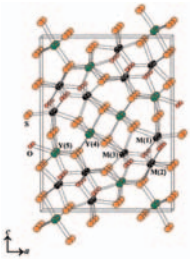

View of the crystal structure of UY4O3S5.

$[Hg_5O_2(OH)_4][(UO_2)_2(AsO_4)_2]$: A complex mercury(II) uranyl arsenate
Yaqin Yu, Kai Jiang and Thomas E. Albrecht-Schmitt
Page 1867

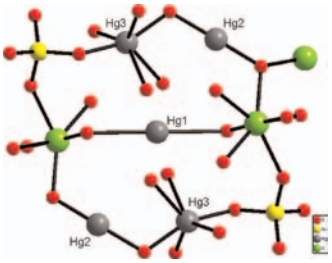

A depiction of the coordination environments for mercury in $[Hg_5O_2(OH)_4][(UO_2)_2(AsO_4)_2]$ (**HgUAs-1**).

Effect of ruthenium substitution in layered sodium cobaltate Na_xCoO_2: Synthesis, structural and physical properties
Pierre Strobel, Hervé Muguerra, Sylvie Hébert, Elise Pachoud, Claire Colin and Marc-Henri Julien
Page 1872

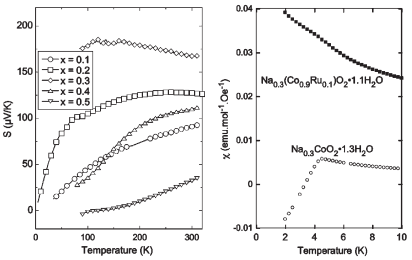

Effect of ruthenium substitution on thermoelectric power in $Na_{0.71}Co_{1-x}Ru_xO_2$ (left) and on low-temperature ac susceptibility in hydrated derivative (right).

Continued

High pressure Raman scattering study on the phase stability of $LuVO_4$

Rekha Rao, Alka B. Garg, T. Sakuntala, S.N. Achary and A.K. Tyagi

Page 1879

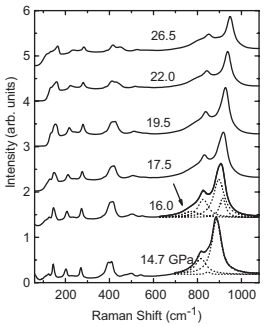

Study of scheelite–fergusonite transition in RVO_4 by Raman spectroscopy is rare. Here we report Raman spectroscopic investigations of $LuVO_4$ at high pressure to obtain insight into nature of post-scheelite phases.

Crystal structure of $BaMg_2Si_2O_7$ and Eu^{2+} luminescence

Cheol-Hee Park and Yong-Nam Choi

Page 1884

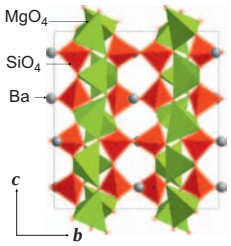

Crystal structure of $BaMg_2Si_2O_7$ projected onto the *bc* plane. The MgO_4 distorted tetrahedra form one-dimensional chains along the unit cell *c*-axis in the structure.

The tunable coordination architectures of a flexible multicarboxylate *N*-(4-carboxyphenyl)iminodiacetic acid via different metal ions, pH values and auxiliary ligand

Xiaochuan Chai, Hanhui Zhang, Shuai Zhang, Yanning Cao and Yiping Chen

Page 1889

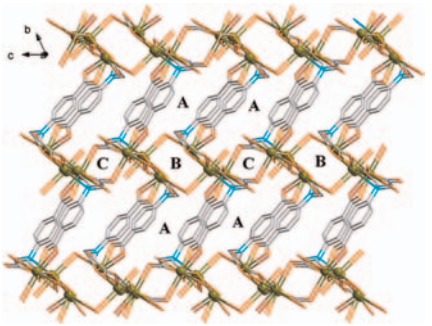

A series of coordination polymers were synthesized with H_3CPIDA and transition metal ions at lower pH values. The figure displays a 3D porous framework with three parallel channels in compound **1**.

Synthesis, crystal structures and properties of three new mixed-ligand d^{10} metal complexes constructed from pyridinecarboxylate and *in situ* generated amino-tetrazole ligand

Dongsheng Liu, Xihe Huang, Changcang Huang, Gansheng Huang and Jianzhong Chen

Page 1899

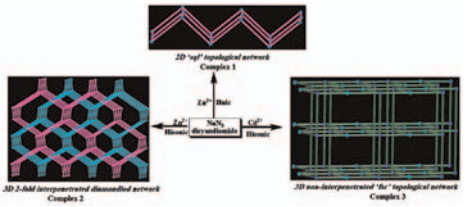

Three new mixed-ligand d^{10} metal complexes have been synthesized by employing mixed-ligand synthetic approach. Complex **1** presents a 2D "*sql*" topological network. Complex **2** is a 2-fold interpenetrated diamondoid network with microporous channels. Rarely observed (4,6)-connected "*fsc*" topological network was found in complex **3**.

Deuterium ordering in Laves-phase deuteride $YFe_2D_{4.2}$

J. Ropka, R. Černý, V. Paul-Boncour and Th. Proffen

Page 1907

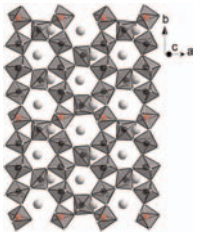

Laves-phase deuteride $YFe_2D_{4.2}$ crystallizes below 323 K in fully ordered monoclinic structure. Seven iron atoms from eight are coordinated by deuterium in a trigonal bipyramid, similar to that in $TiFeD_{1.95-2}$. The eights iron atom is coordinated by deuterium in a tetrahedral configuration.

Two new hydrogen bond-supported supramolecular compounds assembly from tungsten–vanadium polyoxoanions and copper complex fragments

Ji-Wen Cui, Yan Chen, Xiao-Bing Cui, Hai-Hui Yu, Jia-Ning Xu, Ji-Qing Xu, Wei-Jie Duan and Tie-Gang Wang

Page 1913

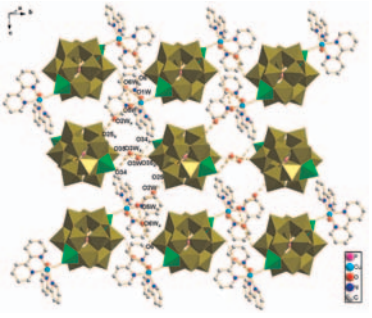

Two new supramolecular compounds were reported. Compounds **1** and **2** exhibit novel 2D supramolecular layer structures constructed from tungsten–vanadium polyoxoanions and different types of secondary building units, respectively.

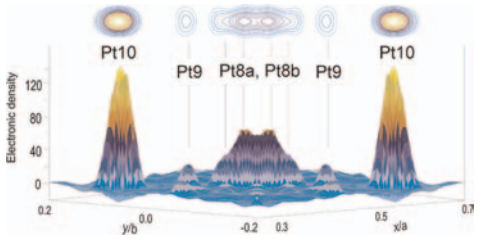

Electron density in $RPt_{3-x}Si_{1-y}$ at 0, $\frac{1}{2}$, 0.

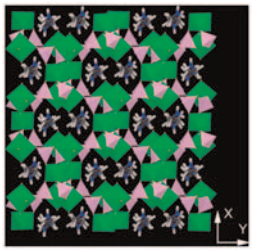

A new three-dimensional iron phosphite with intersecting 6-, 8-, 10-ring channels has been solvothermally synthesized by using diethylenetriamine (DETA) as the structure-directing agent.

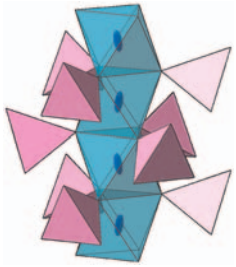

The phase diagram of the system Li_2MoO_4–$ZnMoO_4$ was revised, $Li_{2-2x}Zn_{2+x}(MoO_4)_3$ ($0 \le x \le 0.28$ at 600 °C) isotypical to α-$Cu_3Fe_4(VO_4)_6$ was found. Structural studies for $x = 0$; 0.03; 0.21; 0.23 show consecutive increasing the number of vacancies and atomic displacement anisotropy in the face-shared octahedral columns. Large $Li_2Zn_2(MoO_4)_3$ crystals were grown and their optical, luminescent and scintillating properties were explored.

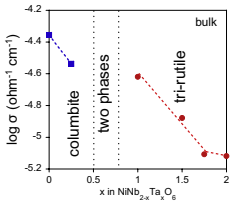

$NiNb_{2-x}Ta_xO_6$ exhibits the columbite structure for low tantalum contents whereas high contents of tantalum stabilize a trirutile-like structure. Electrical conductivity decreases as tantalum content increases in both columbite and tri-rutile.

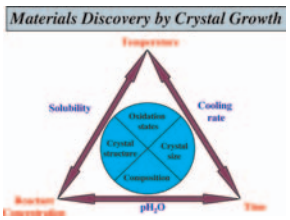

A review that addresses the process of materials discovery via crystal growth using hydroxide fluxes. It provides a detailed overview of the use of hydroxide fluxes for crystal growth and describes the melt chemistry of hydroxide fluxes, specifically, the extensive acid base chemistry, the metal cation solubility, and the ability of hydroxide melts to oxidize metals. In addition, a compilation of complex platinum group metal oxides recently synthesized using hydroxide melts is included.

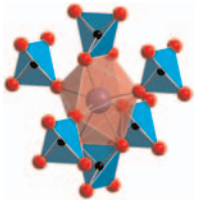

The electronic structures of six vanadate salts, $Ba_3(VO_4)_2$, $Pb_3(VO_4)_2$, YVO_4, $BiVO_4$, Ag_3VO_4 and $CeVO_4$, are studied. The results show that the oxygen to vanadium charge transfer, which is largely responsible for the electronic structure near the Fermi level, can be altered significantly through interactions with the surrounding cations.

Continued

Structural, spectroscopic and magnetic investigation of the $LiFe_{1-x}Mn_xPO_4$ ($x = 0$–0.18) solid solution
Marcella Bini, Maria Cristina Mozzati, Pietro Galinetto, Doretta Capsoni, Stefania Ferrari, Marco S. Grandi and Vincenzo Massarotti
Page 1972

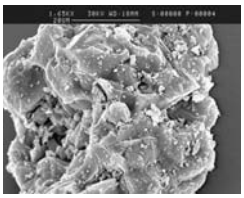

The combined use of different spectroscopic, structural and magnetic techniques has been successfully applied to characterize structure, cation distribution and physical properties of undoped and Mn substituted triphylite and to evaluate the impurity phases formation.

On the magnetic structure of $DyNiO_3$
A. Muñoz, J.A. Alonso, M.J. Martínez-Lope and M.T. Fernández-Díaz
Page 1982

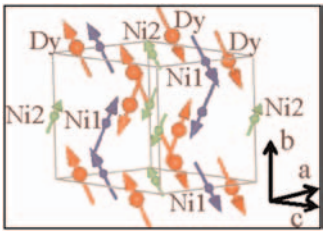

$DyNiO_3$ undergoes a metal–insulator transition at $T_{MI} = 564\,K$. Below T_{MI} the structure is monoclinic with two different sites for the Ni atoms, which present a different valence. It is interpreted as a partial charge disproportionation. Below $T_N = 154\,K$ $DyNiO_3$ orders with an antiferromagnetic structure defined by $\mathbf{k} = (1/2,0,1/2)$.